The Astrophysical Journal, 365:640–647, 1990 December 20

HIGH-RESOLUTION IMAGING AND THE H-R DIAGRAM OF GALACTIC BULGE PLANETARY NEBULAE

M. A. Dopita,[1] J. P. Henry,[2] I. R. Tuohy,[1] B. L. Webster,[3] E. H. Roberts,[4] Y.-I. Byun,[1] L. L. Cowie,[2] and A. Songaila[2]

Received 1990 April 23; accepted 1990 June 8

ABSTRACT

Images of six Galactic bulge planetary nebulae in the [O III] 5007 Å line have been obtained at Mauna Kea at the unprecedented resolution of 0".35 (FWHM), by the technique of real-time photon counting followed by image reconstruction.

The results are compared with those obtained at radio wavelengths, and optical spectrophotometry of the nebulae is used to construct a self-consistent photoionization model, to derive chemical abundances and to place the central stars on the H-R diagram. This method is shown to produce similar results to the classical Zanstra technique, but with the advantage that objects with high- or low-temperature central stars can be studied with equal facility. All our objects are observed during their excursion toward high temperatures on the H-R diagram.

We find that these objects are optically thick, and lie on the good correlation between mass and nebular diameter found by previous authors. We also find a correlation between luminosity and metallicity, which is equivalent to a correlation between metallicity and mass of the planetary nebula nucleus, or between metallicity and stellar age.

Subject headings: nebulae: planetary

I. INTRODUCTION

The study of the evolution of planetary nebulae (PNs) in our solar neighborhood has been plagued by the uncertainties in the distances to these objects. As a consequence, many fundamental parameters remain poorly defined. However, there exist three large samples of planetary nebulae, by the observation of which many of these problems can be overcome. These are the objects in the Large and Small Magellanic Clouds, and the objects lying toward the Galactic center (GC).

The Magellanic Cloud sample has been the subject of a systematic and detailed study in recent years, and data on the diameters, fluxes, expansion velocities, and kinematics have been accumulated (Dopita *et al.* 1985, 1987, 1988; Dopita, Ford, and Webster 1985; Meatheringham *et al.* 1988; Meatheringham, Dopita, and Morgan 1988; Wood, Bessell, and Dopita 1986; Wood *et al.* 1987). This has led to a general understanding of the evolutionary sequence (Dopita and Meatheringham 1990*a*, *b*).

The distance problem has also been largely overcome by observing the objects toward the Galactic center (GC). The increase in numbers is so great that at least 95% of these must lie within 1 kpc of the center of our Galaxy—that is, at a distance of 7.8 ± 1.0 kpc (Feast 1987). The Galactic bulge PNs have been studied mainly by Pottasch and his coworkers (Gathier *et al.* 1983; Pottasch 1987; Pottasch and Acker 1989; Acker *et al.* 1989; Zijlstra, Pottasch, and Bignell 1989). A large number of these have been measured spectrophotometrically by Webster (1988).

Among the physical parameters of planetary nebulae, a fundamental one is the size. Using this, a knowledge of either the flux or the density can be used to derive the nebular mass, and in combination with the velocity of expansion we obtain a dynamical age. In the Magellanic Clouds the determination of the size remains difficult. The smaller objects could only be resolved indirectly by speckle interferometry (Wood, Bessell, and Dopita 1986), and this led to problems in that it tended to resolve only those objects with dense central cores (Dopita and Meatheringham 1990*a*). The alternative method, high-speed seeing-corrected direct imaging, has also been used with some success (Wood *et al.* 1987). However, this can be used only for the largest and most evolved objects.

Although, as a result of their high reddening, the GC sample is not intrinsically very much brighter than the Magellanic Cloud sample, the relative closeness of these objects simplifies determination of their sizes. However, many PNs in the Galactic bulge sample have been determined by objective-prism surveys, and in crowded fields this leads to the detection of the brighter, more compact, and less evolved objects. As a result, about 70% of the sample remain unresolved on photographic plates, and many of the rest of the optically determined diameters are unreliable. Using the VLA, Gathier *et al.* (1983) have produced radio images of 42 objects, and diameters of many more have since been derived (Zijlstra, Pottasch, and Bignell 1989 and references therein).

In order to determine accurate optical diameters, and to determine whether the optical and the radio diameters are similar, we undertook a program of time-resolved seeing-corrected imaging. In this paper we report results of both this ultra–high-resolution imaging and the spectrophotometry for Galactic bulge PNs.

II. OBSERVATIONS

a) Imaging

The imaging observations were carried out on 1988 July 19 and 20 at the Cassegrain focus of the 88 inch (2.2 m) telescope

[1] Mount Stromlo and Siding Spring Observatories, Institute of Advanced Studies, The Australian National University.
[2] Institute for Astronomy, University of Hawaii at Manoa.
[3] School of Physics, University of New South Wales.
[4] Auspace Limited, Canberra.

operated by the University of Hawaii on Mauna Kea. A Barlow lens placed immediately in front of the filter was used to magnify the focal-plane scale to 5".8 mm^{-1}. In order to isolate the light of the planetary nebulae, a 3 inch (7.5 cm) diameter Infra-Red Industries filter was used. This was a three-cycle filter centered at 5010 Å and had a width (FWHM) of 20 Å, which allowed it to isolate the [O III] line at 5007 Å. The detector was the functional model (FM) of the Ultra-Large Photon-Counting Array (Roberts, Tuohy, and Dopita 1988). This is a four-channel intensified CCD photon-counting detector which gave a total format of 1520 × 996 pixels of size 15 × 18 μm. These pixels correspond to 0".088 pixel^{-1} in the east-west axis, and 0".106 pixel^{-1} in the north-south direction. Photons were counted at a frame rate of 65 Hz, and the raw photon event addresses were stored to tape for subsequent image reconstruction.

As a result of the intrinsically excellent seeing of the Mauna Kea site, the isoplanatic patch is large, and, as a consequence, wave-front tilt corrections, which can be thought of as the translational component of the seeing, can be corrected for over quite a large angle, up to 2'. These corrections are large by comparison with the turbulent component of seeing, so dramatic improvements in image quality can be obtained. The translational component can be corrected by forming many short subexposures of an individual object (with exposure times in the range from 40 s up to 120 s), in which high-speed centroiding on a convenient guide star is followed by a shift-and-add process on individual frames. The centroiding or guiding periods were 3, 10, 1, 2, and 1 s for PK 6−3.3, 4−3.1, 359−4.2, 359−2.3, 2−4.1 and 2−6.1, respectively.

The contribution of the translational motions to the seeing in the resultant images clearly depends upon the guiding rate. From experimentation with the data, it was found that this contribution is 0".19, 0".21, and 0".25 for guiding periods of 2.5, 5.0, and 10.7 s, respectively. This error is balanced by the error in the determination of the centroid on what are often faint guide stars. Ignoring the spatial quantization of the detector, the centroid determined from a total of N counts is given by (x, y), where

$$x = \frac{1}{N} \sum_{i=1}^{N} x_i \,, \quad y = \frac{1}{N} \sum_{i=1}^{N} y_i \,.$$

Now, if the variances of x_i, y_i are $\sigma^2(x_i)$ and $\sigma^2(y_i)$, then the variances in the centroid determination $\sigma^2(x)$ and $\sigma^2(y)$ are given by

$$\sigma^2(x) = (1/N)\sigma^2(x_i) \,, \quad \sigma^2(y) = (1/N)\sigma^2(y_i) \,.$$

Thus, it can be seen that only 10 or so photon events from the guide star are required in order to make the error in the centroid determination negligible by comparison with the variances $\sigma^2(x_i)$ and $\sigma^2(y_i)$. However, these are determined by the turbulent component of the seeing convolved with the intrinsic point-spread function of the telescope, and therefore determine the maximum intrinsic resolution that can be obtained in such high-speed imaging.

In order to improve the resolution still further, the fast-guided subexposures were individually deconvolved using the observed profile of the guide star. These images were then co-added through a median filter to produce the final image. The results of this process are presented in Figure 1, which is an observation of a test double star, BD +13°3524, demonstrating a resolution of 0".28 (FWHM). This is somewhat, but only slightly, better than the resolution achieved in the PN observations, where the guide stars were somewhat fainter. We therefore estimate that the typical resolution of our PN images is 0".35 (FWHM).

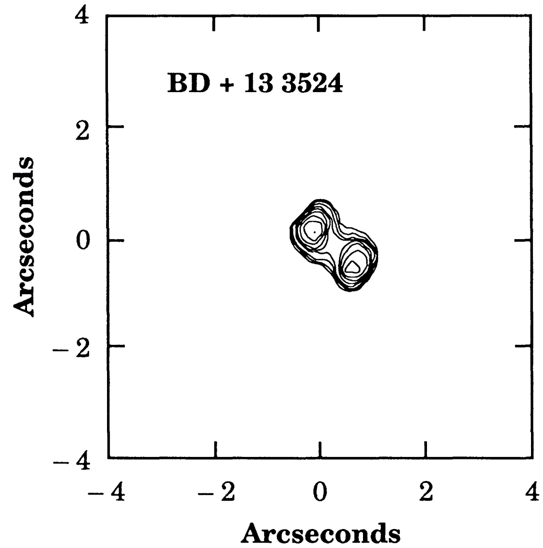

FIG. 1.—Restored image of the double star BD +13°3524 showing the resolution achieved by the image reconstruction technique described in the text. Contours are drawn at the peak divided by 1, 2, 4, 8, 16, 32, 64, 128, and 256.

The images of the individual planetary nebulae are presented in Figures 2*a*–2*e*. The contour intervals are the same for each image, representing 0.95, 0.9, 0.75, 0.5, 0.25, 0.125, 0.0625, and 0.03125 of the value of the pixel with maximum signal. The orientation of each image is the same, and is presented in terms of the x and y coordinates defined by the imager. This is not the standard orientation, however, and directions on the sky are displayed on the upper left-hand image.

Note that not only are the images clearly resolved, but details of the internal structure appear. For example, the majority of the objects appear clearly shell-like. Since all images have more or less sharp outer boundaries, we have measured the diameter at the 25% flux level. In Table 1 we summarize the parameters of the major- and minor-axis diameters, the position angle of the major axis, and, where possible, the shell thickness. This last parameter is estimated from the spatial separation between the outer (25%) boundary, and the position where the shell reaches its maximum brightness,

TABLE 1

MEASURED SIZES OF GALACTIC BULGE PLANETARY NEBULAE[a]

Object (PK)	D_{maj}	D_{min}	P.A.	$\Delta R/R$	D_{maj} (pc)	D_{min} (pc)	D_{radio} G[b]	D_{radio} ZPB[c]
359−2.3	1".9	1".8	65°	...	0.072	0.068	0.7	1.3
359−4.2	3.7	2.5	126	0.28	0.142	0.095	1.3	2.5
2−4.1	2.6	1.8	155	0.37	0.099	0.069	0.65	1.2
2−6.1	5.3	3.8	149	...	0.202	0.145	2.0	4.0
4−3.1	4.1	2.4	146	...	0.156	0.092	...	3.5
6−3.3	2.4	2.0	115	0.33	0.092	0.076	2.1	4.0

[a] Diameters measured to 25% peak flux level.
[b] Gathier *et al.* 1983.
[c] Zijlstra, Pottasch, and Bignell 1989.

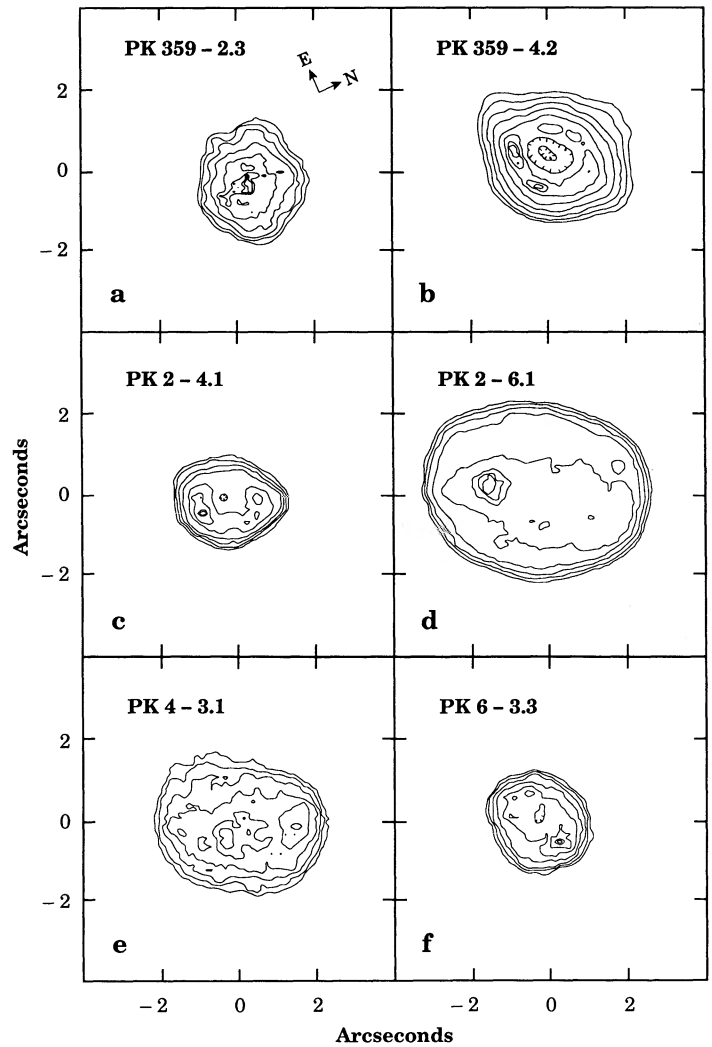

FIG. 2.—(*a–f*) Restored images of the Galactic center observed planetary nebulae. Contours are at the peak times 0.95, 0.9, 0.75, 0.5, 0.25, 0.125, 0.0625, and 0.03125. The images have been stretched in the appropriate direction to produce square pixels on the sky. Contours around central depressions are distinguished by hatching.

which, in a spherical shell model, would be the point at which the line of sight just touches the inner boundary of the nebula.

Note that the optical diameters given in Table 1 agree fairly well with the radio diameters given by Zijlstra, Pottasch, and Bignell (1989), but are systematically larger by almost a factor of 2 than the Gathier *et al.* (1983) estimates. Since the latter are deconvolved by the (fairly large) VLA beam, it suggests that the deconvolution correction has been overestimated. However, it is also clear that our measured diameters are considerably smaller than some of those estimated previously at optical wavelengths. For example, Moreno *et al.* (1988) estimate a diameter of 9″ for PK 2−4.1, and a diameter of 11″ for PK 2−6.1, compared with our median diameters of 2″.2 and 4″.5, respectively.

b) *Spectrophotometry*

Spectrophotometry of all the PNs observed in the imaging program, with the exception of the nebula PK 359−2.3, was obtained on the nights of 1988 May 13 and 14. In the case of PK 359−2.3, we use the data published by Webster (1988). The instrument used was the double-beam spectrograph (DBS) on the 2.3 m telescope at Siding Spring with its 300 line mm^{-1} gratings. With a dichroic beam-splitter cutting at 5500 Å, this gave complete spectral coverage from 3500 to 7800 Å. The detectors were two CCD photon-counting arrays (PCAs) (Rodgers, Conroy, and Bloxham 1988), one for each arm, optimized for blue and red response, respectively. The exposure times were typically 1000 s. However, since the PCA saturates on bright lines, it was also necessary to take additional 1000 s exposures with the telescope defocused and the slit narrow in order to obtain accurate relative fluxes for the brighter lines, particularly the [O III] lines at 4959, 5007 Å. However, as a result of this process the absolute value of the Hβ flux is not reliable and is not given. The data were all reduced using the FIGARO spectral reduction package. Since the data fell on four different CCDs, each of these had to be reduced separately, and then all four combined into a single spectrum. The reduction process consisted of flat-fielding, data extraction, wavelength linearization, sky subtraction, reduction to flux, merging of CCDs, and the summing of rows to extract individual spectra. The data from individual CCDs were merged and flux-calibrated against observed Oke (1974) standard white

TABLE 2

OBSERVED AND REDDENING-CORRECTED LINE FLUXES FOR PLANETARY NEBULAE

λ (Å)	IDENTIFICATION	PK 359−4.2 I_O	PK 359−4.2 I_C	PK 2−4.1 I_O	PK 2−4.1 I_C	PK 2−6.1 I_O	PK 2−6.1 I_C	PK 4−3.1 I_O	PK 4−3.1 I_C	PK 6−3.3 I_O	PK 6−3.3 I_C
3727	[O II]	11.7	44.7	44.9	72.3	21.3	35.8	33.9	70.5	20.4	65.6
3835	H9	2.7	9.0	1.9	3.0	3.2	5.1	6.4	12.4	2.7	7.7
3868	[Ne III]	33.0	105.4	10.5	15.9	20.2	31.6	40.5	76.4	38.9	107.0
3889	H8 + He I	5.4	16.5	8.6	12.8	10.3	15.9	15.3	28.2	7.2	19.0
3967, 3970	[Ne III] + H7	18.4	52.6	7.1	10.3	11.5	17.3	15.6	27.7	20.5	51.2
4026	He I	1.5	3.9	...	...	2.2	3.2	3.0	5.0	1.6	4.0
4069, 4076	[S II]	2.9	7.2	...	...	...	...	...	...	2.1	4.8
4101	Hδ	14.4	34.4	18.0	24.5	18.5	25.9	26.1	42.0	12.3	26.3
4340	Hγ	35.6	65.1	41.2	51.1	36.6	46.2	56.0	77.9	33.7	57.0
4363	[O III]	2.6	4.6	2.0	2.5	...	...	13.4	18.6	4.7	7.8
4471	He I	5.3	8.5	3.5	4.1	3.4	4.1	6.7	8.7	2.9	4.4
4640, 4647	N III, C III	1.6	2.1	...	...	...	...	0.8	0.9	...	...
4686	He II	0.6	0.7	...	...	...	...	...	...	...	...
471, 4713	He I + [Ar IV]	2.9	3.5	1.2	1.3	1.3	1.4	...	...	2.3	2.7
4740	[Ar IV]	3.1	3.7	...	...	...	...	...	...	2.8	3.3
4861	Hβ	100.0	100.0	100.0	100.0	100.0	100.0	100.0	100.0	100.0	100.0
4959	[O III]	418.0	382.3	160.0	155.0	215.7	208.4	136.4	129.9	337.4	312.1
5007	[O III]	...	1100[a]	473.2	447.6	615.7	579.6	425.2	390.4	990.2	864.1
5199	[N I]	3.6	2.6	...	...	...	...	...	...	...	...
5876	He I[b]	88.3	33.8	47.8	34.0	26.5	18.3	67.2	39.8	67.2	29.1
6300	[O I]	29.1	8.0	6.1	3.8	...	...	2.5	1.2	14.9	4.8
6312	[S III]	10.5	2.9	3.0	1.9	...	...	3.6	1.8	6.4	2.1
6363	[O I]	15.9	4.2	2.7	1.7	...	...	3.0	1.4	8.3	2.6
6548	[N II]	309.4	70.8	49.4	29.2	4.9	2.8	22.5	10.1	59.5	16.5
6563	Hα	1257.8	285.0	481.4	285.0	503.2	285.0	642.1	285.0	1037.1	285.0
6584	[N II]	798.3	178.8	131.2	77.1	21.2	11.9	70.0	30.9	319.8	86.8
6678	He I	66.6	13.9	12.6	7.2	7.4	4.0	17.9	7.6	24.6	6.3
6717	[S II]	57.8	12.0	5.6	3.2	1.1	0.6	4.1	1.7	23.5	6.0
6731	[S II]	92.8	19.3	9.6	5.4	2.3	1.2	7.2	3.1	36.4	9.1
7065	He I	76.1	13.0	45.4	24.2	13.5	6.8	41.1	15.7	54.7	11.8
7135	[Ar III]	235.4	39.4	59.1	31.3	26.2	13.1	70.4	26.5	186.8	39.4
7281	He I	4.5	0.7	6.0	1.7	...	...	5.2	1.8	10.5	2.0
7320	[O II]	35.8	5.2	34.9	17.0	2.5	1.2	16.9	5.9	71.0	13.3
7330	[O II]	26.8	3.9	26.6	13.0	2.0	1.0	13.1	4.6	54.8	10.2
7750	[Ar III]	60.5	7.4	20.2	9.6	5.9	2.6	16.9	5.4	51.7	8.3
c Hα)		1.94		0.69		0.75		1.06		1.69	

[a] Line saturated; intensity estimated as 2.88 times the 4959 Å line.

[b] Calibration poor; line intensity unreliable, probably overestimated.

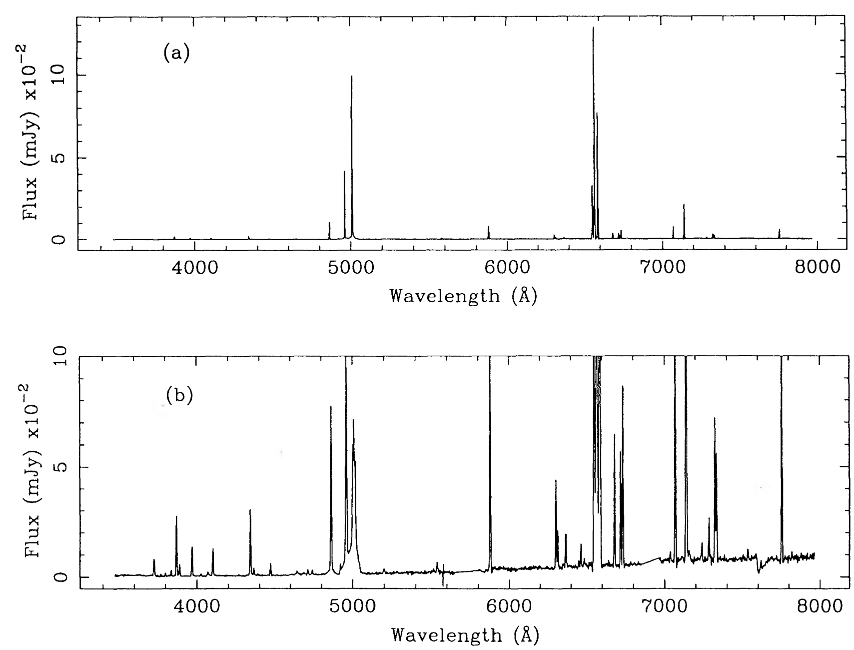

FIG. 3.—DBS spectrum of the planetary nebula PK 359−4.2 obtained (*a*) at low count rate, showing the brighter lines, and (*b*) at high count rate, showing the faint lines and the stellar/nebular continuum.

dwarfs. This process worked well, except at the boundary between the blue detector and the red detector, where the transmission characteristics of the dichroic are changing rapidly. As a consequence, the flux of the 5876 Å He I line is unreliable, and appears, by comparison with the results of Webster (1988), to have been systematically overestimated. The line intensities relative to Hβ are given in Table 2, and a typical spectrum is shown in Figure 3.

III. RESULTS

a) Nebular Masses

Gathier *et al.* (1983) give the following relation for the 6 cm flux:

$$S_{6\ \mathrm{cm}}\ (\mathrm{mJy}) = 0.378 \epsilon N_e^2 (r/\mathrm{pc})^3 (d/\mathrm{kpc})^{-2}\ , \qquad (1)$$

where N_e is the electron density, r is the radius of the emitting source, and ϵ is the filling factor (the fraction of the total volume filled with ionized material). The total mass of the nebula is given by

$$M = \tfrac{4}{3}\pi r^3 \epsilon m_{\mathrm{H}} N_e [1 + 4Z(\mathrm{He})]/[1 + Z(\mathrm{He})]\ , \qquad (2)$$

where m_{H} is the mass of the hydrogen atom and Z(He) is the abundance of helium, by number with respect to hydrogen. In this equation helium is assumed to be singly ionized, which is strictly valid between excitation classes 2 and 5. Hence the total mass of the nebula can be written

$$(M/M_\odot) = 0.16 \epsilon^{1/2} (S_{6\ \mathrm{cm}}/\mathrm{mJy})^{1/2} (r/\mathrm{pc})^{3/2} (d/\mathrm{kpc}) \times [1 + 4Z(\mathrm{He})]/[1 + Z(\mathrm{He})]\ . \qquad (3)$$

From the $\Delta r/r$ values of Table 1, it would seem that a value of $\epsilon = 0.66$ is appropriate in most cases. Adopting a distance of 7.8 kpc (Feast 1987), the mass estimates of Table 3 result. We also give an estimate of the mean density, computed from equation (1), and the density derived from the [S II] λ6717/λ6731 ratio. Note that these two estimates do not agree particularly well. This may be a symptom of the fact that in the nebulae the [S II] ratio is approaching its high-density limit, and therefore density determination suffer from loss of accuracy. Alternatively, it may be the result of radial density and temperature stratification within the nebula. Such fluctuations will ensure that the emissivity of the ion is strongly correlated with regions of high density and high temperature in the zone where the line is produced. In isobaric photoionization models, the [S II] lines arise close to the ionization front, and the mean nebular densities tend to be systematically higher than the [S II] density. However, inspection of Table 3 shows no obvious systematic offset of this kind.

Gathier *et al.* (1983) and, more recently, Pottasch and Acker (1989) have pointed out the strong relationship between nebular mass and nebular radius. They argue, as have Dopita and Meatheringham (1990*a*, *b*), that this relationship is strong evidence in support of the idea that the majority of these PNs are optically thick to the ionizing UV photons produced by the central star. In Figure 4 we compare the relationship found in the Pottasch and Acker (1989) sample with our results. To avoid systematic effects, we have rederived the masses of the Pottasch and Acker sample using equations (1–3) and the figures in their Table 1. There is clearly no significant difference in the mass-radius relationship for the two samples.

TABLE 3

MEAN RADIUS, MASS, AND DENSITY OF PLANETARY NEBULAE

Object (PK)	Radius (pc)	Mass ($M_\odot$)	Electron Density (cm^{-3}) Radio Flux	[S II] Lines
359−2.3	0.035	0.049	13500	15000
359−4.2	0.058	0.126	8300	3500
2−4.1	0.041	0.065	11000	5000
2−6.1	0.086	0.114	2400	7000
4−3.1	0.060	0.055	3400	5900
6−3.3	0.042	0.080	13100	2800

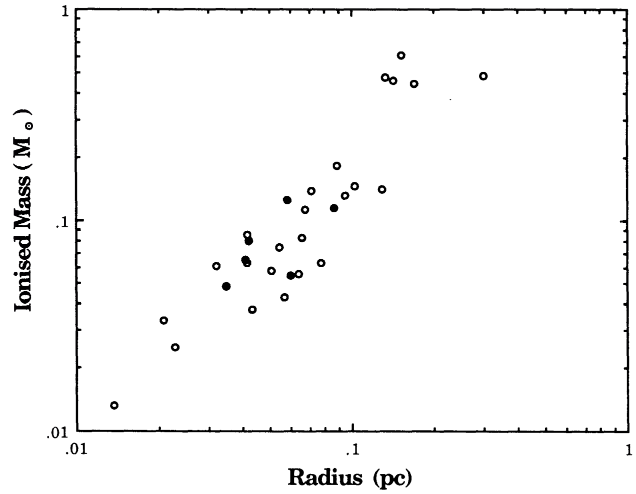

FIG. 4.—Relationship between the nebular mass and the nebular radius. Open circles are based on VLA diameters and fluxes (from Pottasch and Acker 1989), and filled circles are for our measured diameters and using the VLA fluxes.

b) Photoionization Modeling

The determination of the size of these PNs, combined with accurate spectrophotometry over a wide wavelength range, allows a detailed determination of both the nebular abundances and the position of the central star on the H-R diagram. This is possible because, with the aid of a photoionization code, the ionization temperature can be determined from the nebular excitation, the luminosity of the central star can be determined from the density, and the volume of the ionized plasma and the chemical abundances can be determined from the electron temperature and the detailed emission spectrum.

The modeling procedure we adopt is similar to that used for Magellanic Cloud PNs by Dopita and Meatheringham (1990*b*), where a detailed discussion is given. Here we will simply summarize some of the main points. We used the generalized modeling code MAPPINGS (Binette, Dopita, and Tuohy 1985) to compute the emission-line spectra of optically thick isobaric model PNs in photoionization equilibrium. The emission-line spectrum of a photoionized nebula depends upon the chemical abundances, the photon energy distribution, and the ionization parameter (the number of photons crossing unit area per unit time divided by the particle density). In the case of H II regions, Evans and Dopita (1985) and Dopita and Evans (1986) showed that the ratio of [O III]/Hβ is sensitive to all of these. However, in PNs in general, the influence of the ionization parameter is of lesser importance. In this sample of PNs, the mean ionization parameter can in any case be determined from the density, the ionized volume, and the inner radius, all of which are known.

In these photoionization models we have assumed a blackbody photon distribution. This may yield an incorrect excitation, particularly when atmospheric blanketing in He^+ is important, as in the models of Hummer and Mihalas (1970*a*, *b*). However, we find that the blackbody approximation gives a better description of the nebular excitation than photoionization models based on the Hummer and Mihalas atmospheres. The reason may lie in the fact that atmospheric extension due to the stellar wind tends to reduce the blanketing effects and restore the photon distribution toward the blackbody approximation (Gabler *et al.* 1989).

Only PK 4−3.1 has a central star hot enough to produce appreciable ionization of He^{++} in the nebula. For the rest, the excitation temperature has to be determined by the [O III] to Hβ ratio, the [Ne III] to Hβ ratio, and, allowing for the collisional de-excitation of the [O II] lines, the ratio of the [O I], [O II], and [O III] lines. For such nebulae, these are sufficient to fix the blackbody temperature of the ionizing radiation to about ±4000 K. For a given stellar temperature, the abundances determine the electron temperature, and hence the [O III] λ4363/λ5007 ratio. Both the abundances and the temperature of the central star were iterated until the nebular excitation and the nebular temperatures agreed, within the errors, with the photoionization models. For optically thick models, the luminosity of the central star is determined by the radius of the Strömgren sphere (the radius of the ionized region) and the mean nebular density. When the parameters of the photoionization model all agree within the errors of observation and modeling, with the observed parameters of the PNs, the abundances of N, S, Ne, and Ar are fine-tuned to give the best agreement with observation. This point is typically reached after five iterations.

In Table 4 we give the parameters of the "best-fit" models, and in Table 5 the comparison of the observed and modeled line intensities for the most important lines. Based simply on the sensitivity of the model to the input parameters, we estimate that the error in the temperature determinations is ±0.04 dex. The error in the luminosity determination is larger, about ±0.13 dex. This is dependent on the square of the assumed distance to the Galactic center (contribution about ±0.05 dex) and on the errors in the radio flux determination and the diameter measurement (an error of about ±0.08 dex). The formal error in the oxygen abundance is ±0.05 dex, with larger errors for the other elements. However, this error estimate depends upon the accuracy of the atomic data used, and large errors are possible for individual elements. The helium abundances are rather unreliable.

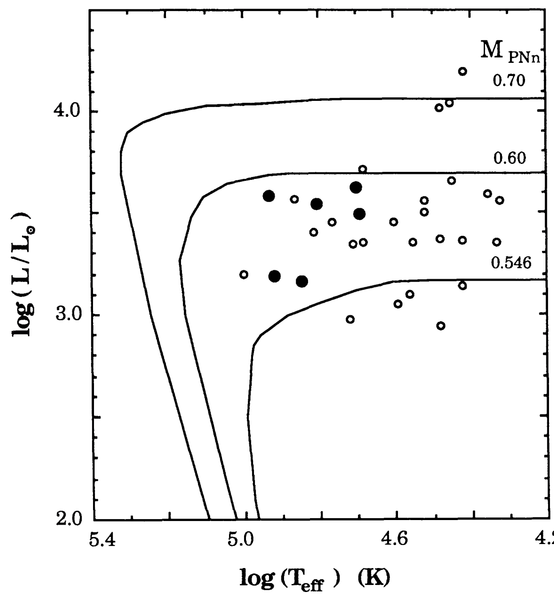

FIG. 5.—H-R diagram for the Galactic bulge PNs. Open circles are based on VLA fluxes and hydrogen Zanstra temperatures, and come from Pottasch and Acker (1989), while filled circles rely on our measured diameters and on excitation temperatures derived from a nebular analysis, as described in the text. Note that our technique is capable of measuring hotter stellar temperatures than the classical Zanstra analysis. The theoretical evolutionary tracks are from Wood and Faulkner (1986) for the 0.6 and 0.7 $M_\odot$ cases, while the 0.546 $M_\odot$ track is from Schönberner (1983).

IV. DISCUSSION

In Figure 5 we give the positions of these PNs on the H-R diagram, compared with the sample of Pottasch and Acker (1989). Their sample has the temperature determined by the classical Zanstra technique and so is strongly biased toward the measurement of lower temperature objects for which the central star may be readily detected against the nebular continuum. The ionization temperature determined from models does not depend on the detection of a central star and so is free of this bias. As a result, it is not surprising that the mean temperature of the central stars in our group of objects is higher than for the Pottasch and Acker (1989) sample.

The mean luminosity of our sample agrees very well with the Pottasch and Acker sample, as indeed it should, since we use their radio continuum measurements in our density determination. We can conclude that the mass range of these PNs is between 0.55 and 0.60 $M_\odot$, although some of the Pottasch and

TABLE 4

PARAMETERS OF PLANETARY NEBULAE DETERMINED FROM NEBULAR MODELS

Object (PK)	$L/L_\odot$	T_{ion} (K)	Chemical Abundances[a] He	N	O	Ne	S	Ar
359−2.3	3500	64000	0.107	5.3E−5	3.3E−4	7.8E−5	7.5E−6	4E−6
359−4.2	3800	86000	0.23	2.8E−4	7.6E−4	1.8E−4	4.0E−5	5E−6
2−4.1	3120	49000	0.15	5.5E−5	3.2E−4	3.5E−5	1.0E−5	5E−6
2−6.1	4170	50000	0.11	7.0E−5	6.9E−4	1.1E−4	2.1E−5	4E−6
4−3.1	1300	80000	0.15	1.3E−5	6.0E−5	2.0E−5	2.5E−6	2E−6
6−3.3	1520	77000	0.15	8.0E−5	2.5E−4	8.0E−5	2.0E−5	5E−6

[a] By number, with respect to hydrogen.

TABLE 5

COMPARISON OF OBSERVED AND MODELED RELATIVE LINE INTENSITIES

λ (Å)	IDENTIFICATION	PK 359−2.3[a]		PK 359−4.2		PK 2−4.1		PK 2−6.1		PK 4−3.1		PK 6−3.3	
		Observed	Modeled	Observed	Modeled	Observed	Modeled	Observed	Modeled	Observed	Modeled	Observed	Modeled
3727	[O II]	...	36	45	45	72	86	36	37	70	36	66	54
3868	[Ne III]	79	80	105	97	16	15	32	23	76	78	107	97
3967, 3970	[Ne III], H7	...	40	53	46	10	20	17	23	28	40	51	46
4069, 4076	[S II]	...	1.5	7	5	...	3	...	0.5	...	1.5	5	5
4101	Hδ	24	26	34	26	24	26	26	26	42	26	26	26
4340	Hγ	47	47	65	47	51	47	46	47	56	47	57	47
4363	[O III]	7	7	5	5	2.5	2.4	1.5	1.3	16	9	8	7
4471	He I	4	5	8	11	4	7	4	5	9	7	4	7
4686	He II	...	...	1	0.6	...	...	...	...	...	0.7	3	0.3
4861	Hβ	100	100	100	100	100	100	100	100	100	100	100	100
4959	[O III]	298	307	382	382	155	153	208	200	130	151	312	280
5007	[O III]	898	885	1100	1000	448	441	580	577	390	434	864	805
5199	[N I]	...	0.3	3	1.3	...	...	...	...	...	0.4	...	0.9
5876	He I[a]	15	15	17	32	18	18	13	15	14	19	29	20
6300	[O I]	3	3	8	4	4	1	...	...	1	1.8	5	4
6312	[S III]	2	1	3	5	2	2	...	...	2	2.3	2	7
6548	[N II]	...	15	71	59	29	25	2.8	4.0	10	11	16	31
6563	Hα	285	285	285	285	285	285	285	285	285	284	285	285
6584	[N II]	44	44	179	173	77	74	12	12	31	32	87	91
6678	He I[b]	4	4	9	9	7	5	4	4	6	5	6	6
6717	[S II]	0.9	1.0	12	7	3.2	2.6	0.6	0.6	1.7	2.0	6.0	6.0
6731	[S II]	2.0	1.9	19	12	5.4	5.2	1.2	0.9	3.1	3.4	9.1	11.1
7135	[Ar III]	17	16	39	21	26	25	13	10	26	12	39	20
7320	[O II]	...	5	5	2	17	6	1	0.6	6	3	13	4
7330	[O II]	...	4	4	2	13	4	1	0.5	5	2	10	3

[a] Line intensities taken from Webster 1988.
[b] Average of Webster 1988 line intensities and values given in Table 3.

Acker (1989) sample may range to higher masses than this. This is narrow, although not so narrow as claimed by Schönberner (1981) or Schönberner and Weidemann (1983) on the basis of a study of the central stars of nearby PNs. Indeed selection effects will ensure that the observed range in mass is smaller than the true range, since rapidly evolving high-mass objects will be located at low luminosity and high temperature, where detection rates are very incomplete.

The very wide range of metallicities found here confirms the results of Webster (1988). Compare, for example, PK 359−4.2 with PK 4−3.1. Webster (1988) finds O/H ratios of 7.8×10^{-4} and 2.8×10^{-5}, respectively. These figures are derived from the ICF method, and compare with the values of 7.6×10^{-4} and 6.0×10^{-5} that we derive by our completely different technnique. The difference in the chemical abundances of these two objects is gross, and is far beyond any possibility of measurement error. Both objects have central stars with similar temperature, so modeling errors would have very little effect on this result. We can therefore conclude that the abundance spread in the Galactic bulge PHs lies from above solar to about 0.1 or 0.05 of solar.

Such a wide range of metallicity can only mean that the objects currently passing through their PN phase in the Galactic bulge were born over a spread of time, both during and after the collapse of the Galaxy. Inspection of Table 5 reveals that there is a good correlation between oxygen abundance and luminosity of the central star (see also Fig. 6). Since all objects are observed in the portion of the H-R diagram where the temperature of the central star is increasing, but where the luminosity is almost constant, this luminosity/metallicity correlation is equivalent to a correlation between mass of the PNs and the metallicity. Provided that this correlation is not masked by the effect of abundance in lengthening the main-sequence lifetime, this in turn can be transformed, through the relation between core mass and stellar age, to an age/metallicity relationship. Thus we have the exciting prospect that the techniques set out in this paper, when applied to a larger sample of objects, can be used to determine the age/metallicity relation for the Galactic bulge region. This would provide an important new observational constraint for models of Galactic collapse.

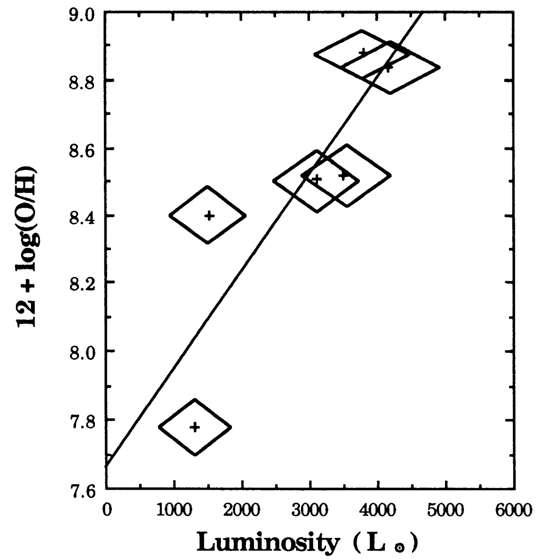

FIG. 6.—Correlation between luminosity and metallicity for our sample. Error diamonds represent the individual PNs, and the straight line is the least-squares linear fit. This is equivalent to a PN mass/metallicity correlation which, provided that the main-sequence lifetime is not too affected by metallicity, may in turn be transformed to an age/metallicity relation for the Galactic bulge.

Hubert Yamada of the Institute for Astronomy wrote the real-time data acquisition software.

REFERENCES

Acker, A., Köppen, J., Stenholm, B., and Jasniewicz, G. 1989, *Astr. Ap. Suppl.*, **80**, 201.
Binette, L., Dopita, M. A., and Tuohy, I. R. 1985, *Ap. J.*, **297**, 476.
Dopita, M. A., and Evans, I. N. 1986, *Ap. J.*, **307**, 431.
Dopita, M. A., Ford, H. C., Lawrence, C. J., and Webster, B. L. 1985, *Ap. J.*, **296**, 390.
Dopita, M. A., Ford, H. C., and Webster, B. L. 1985, *Ap. J.*, **297**, 593.
Dopita, M. A., and Meatheringham, S. J. 1990*a*, *Ap. J.*, **357**, 140.
———. 1990*b*, in preparation.
Dopita, M. A., Meatheringham, S. J., Webster, B. L., and Ford, H. C. 1988, *Ap. J.*, **327**, 639.
Dopita, M. A., Meatheringham, S. J., Wood, P. R., Webster, B. L., Morgan, D. H., and Ford, H. C. 1987, *Ap. J. (Letters)*, **315**, L107.
Evans, I. N., and Dopita, M. A. 1985, *Ap. J. Suppl.*, **58**, 125.
———. 1987, in *Proc. NATO ASI, The Galaxy*, ed. G. Gilmore and R. Caswell (Dordrecht: Reidel), p. 1.
Gabler, R., Gabler, A., Kudritski, R. P., Puls, J., and Pauldrach, A. 1989, *Astr. Ap.*, **226**, 162.
Gathier, R., Pottasch, S. R., Goss, W. M., and von Gorkom, J. H. 1983, *Astr. Ap.*, **128**, 325.
Hummer, D. G., and Mihalas, D. 1970*a*, *M.N.R.A.S.*, **147**, 339.
———. 1970*b*, *JILA Rept.*, No. 101 (Boulder: University of Colorado).
Meatheringham, S. J., Dopita, M. A., Ford, H. C., and Webster, B. L. 1988, *Ap. J.*, **327**, 651.
Meatheringham, S. J., Dopita, M. A., and Morgan, D. H. 1988, *Ap. J.*, **329**, 166.
Moreno, H., Lasker, B. M., Gutiérrez-Moreno, A., and Torres, C. 1988, *Pub. A.S.P.*, **100**, 604.
Oke, J. B. 1974, *Ap. J. Suppl.*, **27**, 21.
Pottasch, S. R. 1987, in *Stellar Evolution and Dynamics of the Outer Halo of the Galaxy*, ed. M. A. Azzopardi and F. Matteucci (Garching: ESO), p. 531.
Pottasch, S. R., and Acker, A. 1989, *Astr. Ap.*, **221**, 123.
Roberts, E. H., Tuohy, I. R., and Dopita, M. A. 1988, *Advances in Electronics and Electron Physics*, **74**, 297.
Rodgers, A. W., Conroy, P., and Bloxham, G. 1988, *Pub. A.S.P.*, **100**, 626.
Schönberner, D. 1981, *Astr. Ap.*, **103**, 119.
Schönberner, D., and Weidemann, V. 1983, in *IAU Symposium 103, Planetary Nebulae*, ed. D. R. Flower (Dordrecht: Reidel), p. 359.
Webster, B. L. 1988, *M.N.R.A.S.*, **230**, 377.
Wood, P. R., Bessell, M. S., and Dopita, M. A. 1986, *Ap. J.*, **311**, 632.
Wood, P. R., and Faulkner, D. J. 1986, *Ap. J.*, **307**, 659.
Wood, P. R., Meatheringham, S. J., Dopita, M. A., and Morgan, D. H. 1987, *Ap. J.*, **320**, 178.
Zijlstra, A. A., Pottasch, S. R., and Bignell, C. 1989, *Astr. Ap. Suppl.*, **79**, 329.

M. A. DOPITA, I. R. TUOHY, and Y.-I. BYUN: Mount Stromlo and Siding Spring Observatories, Private Bag, Weston Creek P.O., ACT 2611, Australia

J. P. HENRY, L. L. COWIE, and A. SONGAILA: Institute for Astronomy, University of Hawaii at Manoa, 2680 Woodlawn Drive, Honolulu, HI 96822

B. L. WEBSTER: School of Physics, University of New South Wales, P.O. Box 1, Kensington, NSW 2033, Australia

E. H. ROBERTS: c/o Matra Espace Instrument Group, 31 rue des Cosmonautes, ZI du Palays, 31077 Toulouse Cedex, France